

# Photoswitchable Gold Nanoparticles for Super-Resolution Radial Fluctuation Imaging in Nanostructured Materials

Julie Probst, Prerit Mathur, Meiyu Gai, Tiejian Si, Qiang He, Changyong Gao, Hanchao Gao, Andrei V Sapelkin, Michael Kappl, Guangyu Qiu, Jing Wang, Johannes Frueh,\* and Stavros Stavrakis\*

Camera-based super-resolution approaches surpass the diffraction limit of conventional optical microscopy by relying on the stochastic activation and precise localization of fluorescent molecules. However, traditional probes such as organic dyes and quantum dots present challenges such as photobleaching and blinking variability, which limit their application in super-resolution imaging, particularly in non-liquid environments. Herein, the study demonstrates the potential of gold nanoparticles as a promising alternative for localization-based super-resolution imaging. The study specifically investigates how different surface functionalizations and states (aggregated vs isolated) of gold nanoparticles impact their photoluminescence properties, including fluorescence intensity, lifetime, and blinking behavior. By leveraging the intrinsic photoluminescence of gold nanoparticles, their capability is demonstrated as probes to achieve super-resolution imaging of nano-sized structures, at a resolution down to 100 nm, without the need for conventional imaging buffers. These proof-of-concept applications, which include imaging of silica nanosized wrinkles and logos, reveal that gold nanoparticles exhibit superior photophysical properties compared to common organic fluorophores, offering a promising alternative for super-resolution imaging. This work paves the way for the application of super-resolution fluorescence microscopy in materials science where non-liquid environments often restrict the use of traditional probes.

## 1. Introduction

The resolution of conventional optical microscopy is generally limited by the diffraction of the light wave when it is focused to a tiny spot.<sup>[1]</sup> More specifically, this is because optical diffraction limits the resolution of an optical microscope to roughly the optical wavelength ( $\lambda$ ) divided by twice the numerical aperture (NA) of the imaging system,  $\lambda/(2NA)$ . This resolution limit in optical imaging has recently been surpassed by several camera based super-resolution fluorescence methods,<sup>[2–5]</sup> including stochastic optical reconstruction microscopy (STORM), super-resolution optical fluctuation imaging (SOFI),<sup>[6]</sup> fluorescence photo-activation localization microscopy (FPALM)<sup>[7]</sup> and photoactivated localization microscopy (PALM).<sup>[2,3,5]</sup> These approaches are based on the precise localization of single fluorophores through a switching/activation stochastic process between

J. Probst, P. Mathur, S. Stavrakis  
Institute for Chemical and Bioengineering  
Department of Chemistry and Applied Biosciences  
ETH Zürich  
Vladimir Prelog Weg 1, Zürich 8093, Switzerland  
E-mail: [stavros.stavrakis@chem.ethz.ch](mailto:stavros.stavrakis@chem.ethz.ch)

M. Gai, M. Kappl  
Max-Planck-Institut für Polymerforschung  
Ackermannweg 10, 55128 Mainz, Germany

M. Gai, A. V Sapelkin  
School of Engineering and Materials Science  
Queen Mary University of London  
Mile End, Eng, 215, London E1 4NS, UK

T. Si  
Physics Department  
School of Physics  
Harbin Institute of Technology  
Yikuang Street 2 2H, Harbin 150080, P. R. China

Q. He, C. Gao, J. Frueh  
Key Lab of Microsystems and Microstructures Manufacturing  
Harbin Institute of Technology  
Yikuang Street 2 B1, Harbin 150080, P. R. China  
E-mail: [johannes.frueh@alumni.ethz.ch](mailto:johannes.frueh@alumni.ethz.ch)

C. Gao  
Ningbo Institute of Materials Technology and Engineering  
Chinese Academy of Sciences  
Ningbo 315201, P. R. China

H. Gao, G. Qiu, J. Wang, J. Frueh  
Institute of Environmental Engineering  
Department of Civil  
Environmental and Geomatic Engineering  
ETH Zürich  
Zürich 8093, Switzerland

H. Gao, J. Wang  
Advanced Analytical Technologies Laboratory  
EMPA  
Überlandstrasse 129, Dübendorf 8600, Switzerland

 The ORCID identification number(s) for the author(s) of this article can be found under <https://doi.org/10.1002/smt.202401411>

DOI: 10.1002/smt.202401411

bright (fluorescent) and dark states.<sup>[8]</sup>

Until now, organic dyes, quantum dots (QDs), and photoswitchable proteins have been used as probes for localization-based super-resolution imaging.<sup>[9,10]</sup> Organic dyes (such as Alexa 647) exhibit inherent blinking properties; however, they are very sensitive to their environment and usually undergo photobleaching in the presence of oxygen. Consequently, these dyes necessitate the use of oxygen-scavenging imaging buffers, which can alter the pH of the sample over time, leading to sample degradation and a reduction in dye brightness.<sup>[11–13]</sup> QDs are attractive probes due to their high photon yield, yet their application in localization/fluctuation-based super-resolution microscopy remains problematic due to their blinking frequency variation,<sup>[10]</sup> and large photoswitching ( $t_{\text{on}}/t_{\text{off}}$ ) ratio. Commercially available cadmium-based QDs are typically coated with thick shells and polymeric coatings, which render them up to 15–20 nm in size. These coatings, while enhancing both brightness and chemical stability, tend to also reduce blinking so that the QDs spend most of the time in the “on” state with only brief periods in the “off” state. Despite these limitations, various localization analysis methods have been recently developed for super-resolution QD localization based on the blinking of quantum dots, such as Quantum Dot Blinking with three-dimensional (3D) imaging (QDB3),<sup>[14]</sup> SOFI,<sup>[6]</sup> Bayesian localization<sup>[15]</sup> and non-negative matrix factorization with iterative restarts (iNMF).<sup>[16]</sup>

One of the most popular localization-based super-resolution imaging approaches is STORM-which can be performed by illuminating the sample with a single-color laser, performing activation, excitation, and photoswitching of the fluorophore.<sup>[17]</sup> This approach has been achieved with a large variety of dyes spanning a broad color spectrum, and is referred to as direct (d)STORM.<sup>[17]</sup> In general, photoswitchable probes are a hallmark of this technique. The probes can be categorized into three different groups, 1) reversibly switchable probes, which cycle between a fluorescent (on) and a dark (off) state,<sup>[9]</sup> 2) irreversible photoactivatable probes<sup>[18]</sup> and 3) photobleaching probes according to the bleaching/blinking mechanism.<sup>[4]</sup> In addition to photoswitchable probes, on/off switching of molecules can be performed by reversible ligand binding<sup>[19]</sup> or by quenchers.<sup>[20]</sup> The most common probes for single molecule localization microscopy are switchable fluorescent proteins and organic dyes. Fluorescent proteins offer exceptional target molecule specificity; however, their low photon yield results in inferior localization precision compared to organic dyes. Organic dyes, on the other hand, provide adequate blinking frequency and photon emission to function as photoswitchable probes for super-resolution imaging, but only when utilized within specific imaging buffers. As a result, these methods are not applicable in non-liquid environments typically encountered in materials science characterization. This limitation is reflected in the relatively small number of studies reporting new classes of fluorophores designed to advance super-resolution fluorescence microscopy in materials science.<sup>[21–23]</sup> Therefore, the primary challenge in broadening the scope of super-resolution imaging applications lies in the development of switchable probes with appropriate photophysical and chemical characteristics, such as high photostability, excellent blinking properties, independence from sample environment and being commercially available.

Photoluminescence (PL) of metals was first reported in 1969 by Mooradian,<sup>[24]</sup> and more recently Geddes et al reported the luminescent and blinking behavior of gold nanoparticles (AuNPs).<sup>[25]</sup> Although the quantum yield (QY) of AuNPs is still several orders of magnitude lower than that of fluorescent organic dyes, their large absorption cross section compensates for their low QY, rendering them suitable as high-contrast imaging agents. Thus, the luminescence of AuNPs has been successfully used in the imaging of cells<sup>[26]</sup> and diagnostics.<sup>[27]</sup> In addition they exhibit high photostability<sup>[28]</sup> and time-dependent emission intensity (blinking behavior). While plasmonic AuNPs have been utilized as excellent alternatives to organic fluorescent moieties and QDs to achieve image contrast, their utility as photoswitchable probes for localization-based super-resolution-fluorescence microscopy remains underexplored although they have been previously reported to blink and emit fluorescence.<sup>[25,29]</sup>

In this work, we examine the behavior of AuNPs as reversibly photoswitchable probes and demonstrate for the first time their use for super-resolution imaging. More specifically we investigate how their surface functionalization with different groups and inter-particle distance influence the two most important properties of super-resolution imaging: number of photons per switching event and on/off duty cycle (the fraction of time a fluorescent probe spends in the “on” state).<sup>[30]</sup> By employing the intrinsic luminescence of AuNPs, which is highly dependent on the surface functionalization, super-resolution imaging can be achieved without the use of redox buffers typically used to enhance the photoswitching properties of dyes. We examined AuNPs with two different types of surface functionalization: citrate, and positive branched-polyethylenimine (BPEI) capping, and compared their photophysical properties with plasma-cleaned AuNPs. We also implemented two different sample preparation procedures to investigate the effect of plasmonic interactions on the photophysical properties of these types. More specifically, these procedures enabled the preparation of two distinct particle arrangements: widely spaced particles (sample termed “isolated”, **Figure 1a**) and particles with short inter-particle distances that allow for plasmonic interactions (sample termed “aggregated”, **Figure 1b**). A rigorous evaluation of different parameters such as types of surface functionalization and nanoparticle interactions (aggregated vs isolated) was conducted to assess their impact on the photoluminescence properties (fluorescence intensity and lifetime) and blinking behavior of AuNPs. This analysis identified the optimal conditions to meet the requirements for super-resolution imaging. Subsequently, we demonstrated that super-resolution imaging of patterned sub-diffraction lines can be achieved at a resolution down to 100 nm based on the photoswitching behavior of the selected type of AuNPs.

## 2. Results and Discussion

### 2.1. Photophysical Properties of Gold Nanoparticles and Aggregates

We first investigated the absorbance and photoluminescence spectra of isolated and aggregated AuNPs (**Figure 1a**) by drop-casting a liquid suspension of these NPs on a glass slide. In the case of the isolated samples, the particle-particle distance is

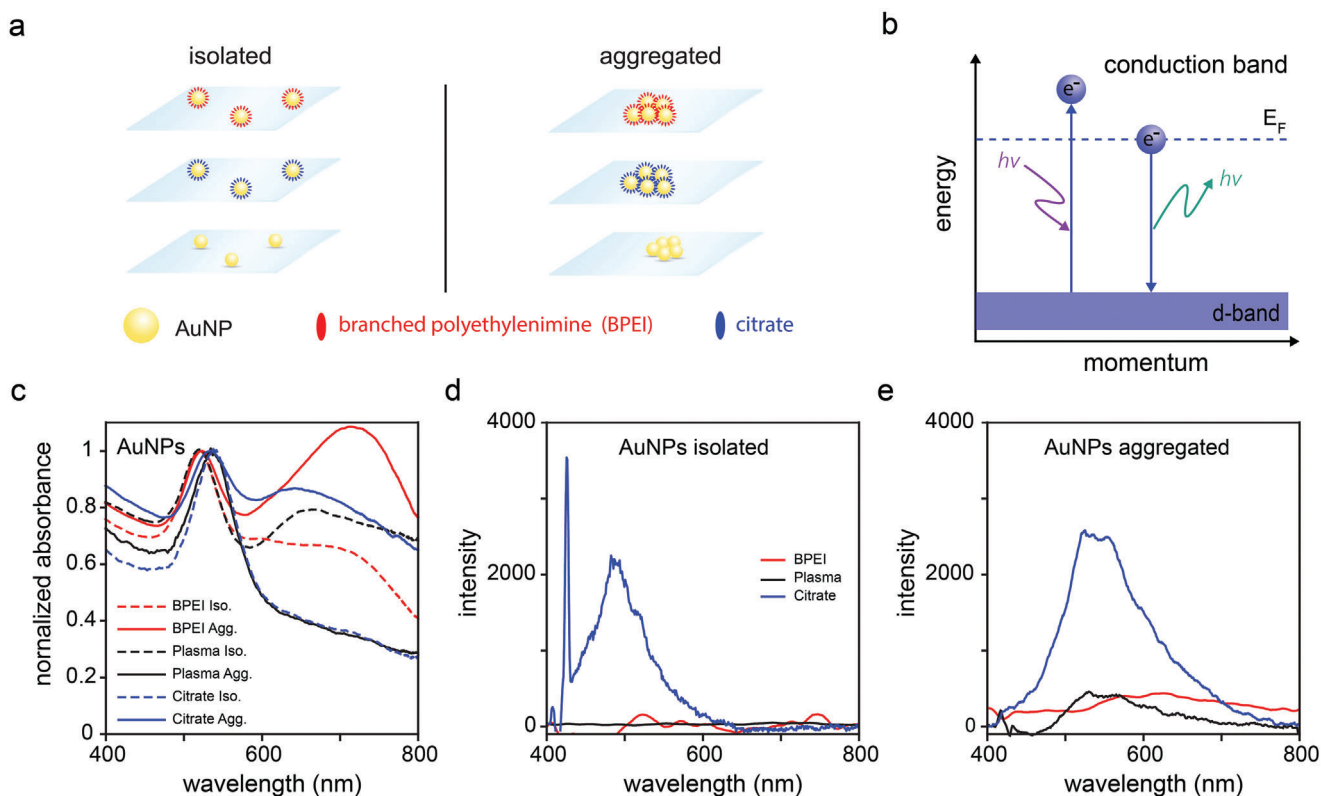


**Figure 1.** Optical properties of AuNPs (40 nm diameter) with different surface functionalizations. a) Schematics of the different AuNPs samples deposited on glass slides and decorated with negative (citrate) or positive (BPEI) surface groups and no surface functionalization (plasma cleaned). b) Electronic band structure of AuNPs, showing how electrons can get excited above the Fermi level and emit photons as they relax to the d-band state. c) Absorption spectra of the AuNP samples in isolated (dotted lines) or aggregated (full lines) state. d) Emission spectra of isolated AuNPs with different surface functionalizations. e) Emission spectra of aggregated AuNPs with different surface functionalizations. The excitation wavelength was 405 nm for the emission spectra.

larger than the plasmonic interaction distance while for the samples containing aggregated NPs, the particle's proximity enables strong plasmonic interactions (Figure S1, Supporting Information). For each of these samples, either in an isolated or an aggregated state, we used two different surface functionalizations, a negatively charged citrate capping, and a positive BPEI network, and no surface functionalization termed as “plasma cleaned.” Plasma cleaned surfaces of AuNPs were investigated via Raman spectroscopy to confirm the successful removal of any surface groups (Figure S2, Supporting Information).

Noble metals, in particular AuNPs, have electronic band structures, which include a set of valence bands with low dispersion, called *d*-bands (composed of electron levels originating from the atoms' *d*-orbitals), and a half-filled *sp*-band called the conduction band.<sup>[24,31]</sup> All the electron bands can be either filled or empty, except for the conduction band which is filled up to the Fermi level.<sup>[24]</sup> The response of Au to an electromagnetic excitation in the UV–vis range cannot be solely described in terms of the behavior of the quasi-free conduction electrons (*sp*-band), but must include the influence of bound electrons in the *d*-bands.<sup>[31]</sup> The schematic in Figure 1b illustrates the light-matter interactions of AuNPs when the excitation energy is matched with their intrinsic interband transition energy.<sup>[24]</sup> This transition involves *d*-band electrons being excited above the Fermi level (into the *sp*-

band), and then relaxing back to the *d*-band states by emitting photons.<sup>[32]</sup> When the excitation wavelengths are in the range between 400 and 500 nm, bound electrons can get excited above the Fermi level,<sup>[31]</sup> or alternatively perform interband transitions from *5d* to *6sp* – from filled bands to conduction band states, or from the latter to empty bands of higher energy.<sup>[33]</sup>

In the current study, we used AuNPs larger than 20 nm, that have an absorption spectrum that combines contributions from both absorption and scattering modes, with their relative contributions varying based on particle size.<sup>[34]</sup> More specifically the absorption in the short wavelength region is due to gold interband electron transitions between the *5d* and *6sp* conduction bands. The absorption spectra of AuNPs with different surface functionalization are illustrated in Figure 1c where surface functionalization with negatively charged citrate groups causes a significant red-shift. This is consistent with the work of Peng et al who demonstrated that by chemically tuning the conductivity of the outer layer in metal NPs through a ligand exchange process, a significant redshift on the surface plasmon resonance band was observed.<sup>[35]</sup>

Figure 1c reveals that the absorbance spectra of BPEI-functionalized AuNPs in the isolated state display no spectral shift in the plasmon band compared to plasma-cleaned AuNPs. However, when BPEI-functionalized and plasma-cleaned AuNPs

are in their aggregated state, the plasmon absorption bands exhibit a redshift. Additionally, the plasmon band becomes wider, and the absorption in the 600–800 nm range increases compared to the spectra of isolated particles (Figure 1c). This can be explained by the fact that at low densities, individual particles are sufficiently separated, preventing any interaction among them. In this state, the electric field created around each particle by the excitation of a surface plasmon is not felt by other surrounding particles. However, when aggregation occurs, the interparticle distances become smaller than the plasmonic field, causing the plasmonic fields of two or more particles to interact.<sup>[36]</sup> This interaction induces coupling between the plasmon oscillations of adjacent nanoparticles, altering their localized surface plasmon resonance wavelength. Interestingly, no significant spectral shift is observed for the aggregated citrate-functionalized AuNPs but the fact that the plasmon resonance band becomes wider (Figure 1c) indicates aggregation albeit at a low percentage.

The PL behavior of AuNPs can provide information about the structure and influence of the ligands on metal cores. According to the plasmon modulated emission model, PL originates from the radiative electron-hole recombination, which is significantly influenced by plasmon resonances. Initially, a 405 nm photon excites electrons from the *d*-band into the *sp*-band elevating them well above the Fermi level. Subsequently, the hole in the *d*-band undergoes Auger scattering and hole-phonon scattering, followed by direct recombination of a *d*-band hole with an electron in the *sp*-band below the Fermi level, generating a particle plasmon. In the final step, the particle plasmon decays radiatively. Figure 1d,e show PL emission spectra recorded for different isolated and aggregated AuNPs under excitation at 405 nm, chosen to fall within the inter-band transition energy domain of Au. At this excitation wavelength, PL emission from BPEI (red line) and plasma cleaned (black line) AuNPs were not measurable since their PL intensities are below the detection limit of the spectrometer (Figure 1d,e). This agrees with previously investigated low intensity emission spectra of unannealed AuNPs films.<sup>[37]</sup> This is also in agreement with a recent study on the PL emission properties of PEI AuNPs.<sup>[38]</sup> On the other hand, PL spectra of citrate-coated isolated and aggregated AuNPs (blue lines) showed a significantly stronger PL signal compared to their plasma-cleaned counterparts (Figure 1d,e) underlining the importance of the negative surface charge to the photoluminescence properties. These results indicate that photoluminescence is enhanced by the transfer of charge from the surface ligands (such as citrate which are electron donating groups) to the metal core. This is consistent with previous reports that support the mechanism in which electron-rich functional groups can enhance luminescence through capping-core interactions, specifically via charge transfer from the ligands to the metal nanoparticle core through the Au-S bonds.<sup>[39]</sup> The PL emission in the case of BPEI-coated (Figure 1d, red line) AuNPs is considerably weaker than that of citrate-coated, suggesting that fewer ligand-core interactions contribute to the PL emission signal. In the case of the plasma-cleaned AuNPs (black line), the absence of surface functionalization allows atmospheric oxygen to directly interact with the NP surface. This interaction can quench its photoluminescence, as the free electron pairs of oxygen act as electron acceptors.<sup>[33]</sup>

In all cases, aggregated AuNPs exhibited an enhanced PL signal, and a redshift of the PL peak (Figure 1e) compared to those

in the isolated state. This finding highlights the importance of plasmonic interaction since particles in close proximity exhibit stronger plasmonic interactions and thus enhancement of the PL signal.<sup>[40,41]</sup> Among the aggregated AuNPs, citrate-functionalized aggregated particles showed the strongest emission and a significant redshift compared to isolated NPs (Figure 1d,e).

The observed dependence of light emission intensity on surface functionalization together with the high Stoke's shift (more than 50 nm) can be explained by the fact that electrons above the Fermi level (termed "hot" electrons)<sup>[42]</sup> interact with surface functional groups.<sup>[33]</sup> These observations suggest a strong influence of NP surface on its PL behavior, governed by ligand-to-metal charge transfer transitions. It is worth noting that AuNPs possess a higher extinction coefficient<sup>[43]</sup> than most organic dyes enabling them to harvest more light. However, their quantum yield is also significantly lower (up to orders of magnitude) compared to organic dyes, and therefore the total emission intensity is not significantly higher compared to organic dyes.

To further analyze in detail how fluorescence properties of isolated and aggregated AuNPs are influenced by different types of surface functionalization, time-resolved fluorescence spectroscopy was implemented, at 405 nm excitation which ensures electron excitation above the Fermi level. Time-resolved spectroscopy techniques like time-correlated single photon counting (TCSPC) measure the photoluminescence lifetime ( $\tau$ ), which is the average time a fluorophore remains in the excited state before returning to the ground state. In all cases and all nano species (NPs and nanorods (NRs)), time-resolved measurements can be fitted to a tri-exponential decay curve, indicating the presence of three distinct processes contributing to the PL signal. This suggests the presence of three different lifetimes to each of which a certain amplitude can be assigned. The PL lifetimes were extracted using the equation:

$$I(t) = A_1 e^{-t/\tau_1} + A_2 e^{-t/\tau_2} + A_3 e^{-t/\tau_3} \quad (1)$$

where  $I(t)$  is the total detected photon intensity,  $t$  is the time and  $A_i$  is the amplitude associated with each decay time,  $\tau_i$ . Table 1 lists the PL lifetime components,  $\tau_1$  and  $\tau_2$  and  $\tau_3$  as well as normalized pre-exponential parameters,  $A_1$ ,  $A_2$  and  $A_3$  obtained from the fitting. In all cases, there is a process characterized by the lifetime constant  $\tau_1$  ranging within a few picoseconds (ps), a second process ranging within 400–700 ps with a time constant,  $\tau_2$ , and a third process with a time constant  $\tau_3$  which extends more than 3 ns. The extremely fast component ( $\tau_1$ ) has a major amplitude between 74% and 98%, while the slower component ( $\tau_2$ ) has a lower contribution in amplitude between 3 and 22%.

In general, AuNPs have been characterized by very short, almost instantaneous lifetimes which are less than the instrumental response function (IRF) ( $\approx 35$  ps) of ultrafast systems.<sup>[44]</sup> Previous analyses of gelatin-coated  $\approx 80$  nm spherical AuNPs inside ovarian cancer cells revealed a single-decay photoluminescence with a time constant of  $\leq 100$  ps.<sup>[45]</sup> On the other hand, it was observed that the PL decay can vary from 0.8 to 2 ns depending on the size and shape of AuNPs.<sup>[46]</sup> Based on the above, the two decay times in the ps time domain can be attributed to both light scattering occurring from the surface of the AuNPs and coupling

**Table 1.** PL Lifetime data for the different samples. The lifetime components,  $\tau_i$ , are reported with their normalized pre-exponential factors,  $A_i$ .

| Sample                      | $A_1$ | $A_2$  | $A_3$  | $\tau_1$ [ns] | $\tau_2$ [ns] | $\tau_3$ [ns] | $\tau_{ave}$ [ns] |
|-----------------------------|-------|--------|--------|---------------|---------------|---------------|-------------------|
| BPEI AuNP iso.              | NA    | NA     | NA     | NA            | NA            | NA            | NA                |
| BPEI AuNP agg.              | 0.969 | 0.026  | 0.005  | 0.023         | 0.675         | 4.14          | 0.059             |
| BPEI AuNR iso.              | 0.976 | 0.020  | 0.003  | 0.019         | 0.403         | 3.65          | 0.037             |
| BPEI AuNR agg.              | 0.736 | 0.222  | 0.041  | 0.060         | 0.695         | 3.80          | 0.354             |
| citrate AuNP iso.           | 0.870 | 0.123  | 0.009  | 0.037         | 0.371         | 3.645         | 0.111             |
| citrate AuNP<br>agg.        | 0.872 | 0.110  | 0.018  | 0.062         | 0.686         | 3.53          | 0.192             |
| plasma cleaned<br>AuNP iso. | NA    | NA     | NA     | NA            | NA            | NA            | NA                |
| plasma cleaned<br>AuNP agg. | 0.999 | 0.0008 | 0.0002 | 0.007         | 0.544         | 3.25          | 0.008             |

between surface plasmons and luminescence.<sup>[46]</sup> It is worth noting that since the decay time of the  $\tau_1$  component is lower than the IRF of our TCSPC system (50 ps FWHM), its value cannot be accurately determined. Nevertheless, the trends obtained from the lifetime data remain valid. These extremely fast decay times have been attributed to the radiative decay of surface plasmons generated from excited electron–hole pairs following interband absorption. This mechanism proposes the excitation of a surface plasmon by an excited electron–hole pair, where the electron–hole pair is initially created either through direct excitation (i.e., interband transitions) or from the decay of an excited plasmon.<sup>[47]</sup> The slow component in the ns domain ( $\tau_3$ ) having an exceptionally low contribution for all samples (between 0.5 and 1.8%) may arise from the glass surface impurities, since it was present in all measurements.

The PL decay times of isolated plasma-cleaned and BPEI-functionalized AuNPs could not be measured due to the time resolution limit of the TCSPC system (IRF: 50 ps FWHM). As a result, a direct comparison of PL lifetimes between isolated and aggregated BPEI-functionalized AuNPs was not feasible (Figure 2a). To address this, we measured the lifetimes of BPEI isolated and BPEI aggregated gold nanorods (AuNRs) (Figure 2b,c). Unlike NPs, NRs typically exhibit weaker photoluminescence and thus longer PL lifetimes that are within the detectable range of our TCSPC setup (Figure S3, Supporting Information). This allowed us to effectively compare the PL lifetimes of isolated versus aggregated species, showing that aggregation increases the average PL lifetime. Specifically, BPEI aggregated AuNRs showed a longer average lifetime of 0.354 ns whereas BPEI isolated AuNRs exhibited a much shorter average lifetime of 0.037 ns (Figure 2b,c and Table 1).

In contrast to isolated particles, aggregation significantly increases the lifetimes of AuNPs and AuNRs, highlighting the complex nature of the PL emission mechanisms. In fact, both AuNPs and NRs aggregates show enhanced PL emission compared to the isolated species (Figures 1 and S3, Supporting Information). As mentioned previously, PL in metal films primarily originates from radiative recombination between conduction band electrons and valence band holes,<sup>[24]</sup> with AuNPs exhibiting enhanced PL due to surface plasmons.<sup>[48]</sup> Furthermore, recent studies on Au-thiolate nanoclusters further emphasize that aggregation enhances PL intensity, which varies with the extent

of aggregation.<sup>[49]</sup> Herein, despite the significant PL intensity enhancement of BPEI AuNR aggregates (Figure S3, Supporting Information), there is a substantial increase in the PL lifetime compared to the isolated state. Such a PL lifetime increase in aggregated nanocrystals has been described earlier<sup>[50]</sup> and was attributed to changes in the local refractive index of the surrounding medium when going from the isolated to the aggregated state. Similar to the BPEI case, the  $\tau_1$  and  $\tau_2$  lifetime components of the citrated AuNP samples reveal faster PL decays in the isolated state compared to the aggregated one (Figure 2d,f, and Table 1). Additionally, both BPEI and citrate-functionalized AuNPs in the aggregated state show distinct average lifetimes (Figure 2a,g and Table 1) indicating significant variations in surface-core interactions governing fluorescence decay processes.

To analyze how these surface functionalizations affect the photophysical properties, we measured the lifetimes of plasma cleaned AuNPs (Figure 3f). Typically, in the case of a smooth gold surface (plasma cleaned), the PL emission exhibits a low efficiency from transitions between  $5d$  and  $6sp$  bands. The average lifetime of plasma cleaned isolated AuNPs could not be measured with our existing time resolution (IRF: 50 ps FWHM) but the citrate functionalization caused a significant lengthening of the average lifetime to 111 ps. Looking at the individual lifetimes (Table 1) it is clear that the ps timescale processes have the highest contribution to the lifetime change (75–98%) upon functionalization, compared to the slower one (>3ns). We attribute the lengthened lifetime to the effect of functionalization which contributes to the photoluminescence through ligand-metal charge transfer interactions. The low QY typically found in metal NPs has its origin in the existence of non-radiative processes. QY of AuNPs can be enhanced via charge transfer from the ligands to the metal core (i.e., LMCT) through the Au–S bonds and is analogous with the ligand’s capability of donating electron density to the metal core through the S–Au bond. Thus, the capping effect of the citrate, and more specifically the charge transfer from the citrate electron-rich groups to the metal core (through the Au–S bonds), enhances the radiative processes thus increasing the QY.

In addition to understanding PL characteristics, assessing the blinking behavior of all the aforementioned AuNPs bearing different chemical surface functionalizations is crucial for their application as photoswitchable probes in super-resolution imaging. To evaluate this, we recorded blinking time traces over 1100

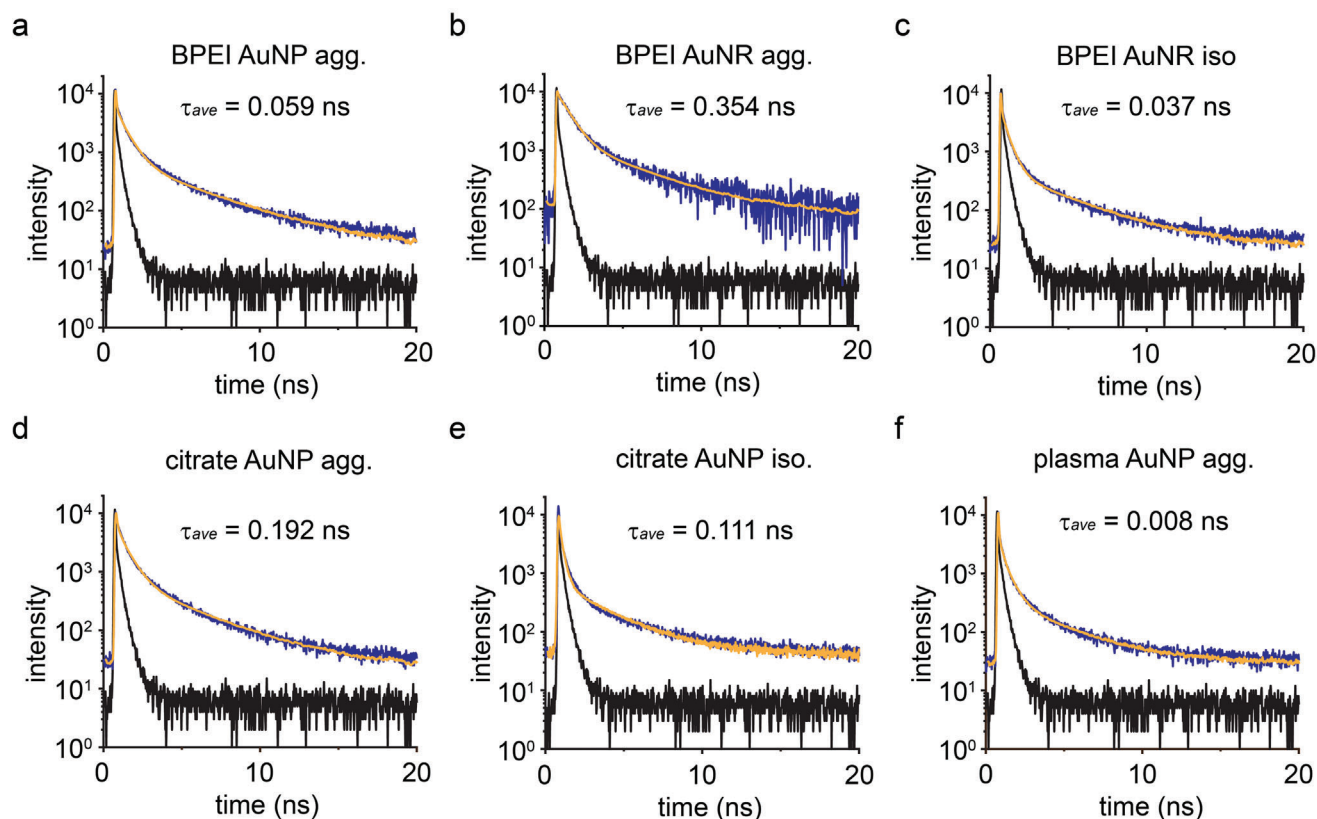


**Figure 2.** Normalised photoluminescence (PL) decays of gold nano-species. a) PL decays of BPEI-capped aggregated AuNPs, b) aggregated AuNRs, and c) isolated AuNRs. d) PL decays of citrate-capped aggregated, e) isolated, and f) plasma-cleaned aggregated AuNPs. The black curves are the IRFs, blue lines are the experimental photoluminescence decay curves, and the yellow lines correspond to tri-exponential fits.

seconds using objective-based total internal reflection fluorescence (TIRF) or highly inclined and laminated optical sheet (HILO) imaging modes (Figure 3) and extracted switching properties such as the on-off duty cycle (or the fraction of time a fluorophore spends in the on-state), and the number of photons detected per switching event. Ideally, a probe with a high photon yield per switching event and a low duty cycle provides high localization precision and is thus able to resolve small structures. A fluorophore with a low photon yield can only be localized with low precision and a high on/off duty cycle limits the density of probes that can be localized within a diffraction-limited area.

Among all tested conditions and functionalizations, only aggregated AuNPs whether functionalized or plasma-cleaned (Figure 3a–c) exhibited strong intensities during blinking. Specifically, BPEI-AuNPs exhibited the highest mean photon intensities at 9828 counts, followed by citrate-AuNPs at 6240 counts. Additionally, these aggregates showed similarly low on/off duty cycles: BPEI-AuNP at  $9.2 \times 10^{-4}$ , citrate-AuNP at  $8.7 \times 10^{-4}$ , and plasma cleaned AuNPs at  $1.6 \times 10^{-4}$ . Aggregated plasma cleaned AuNPs display detectable blinking with low mean photon number per switching event (1932 counts) compared to BPEI- and citrate-AuNPs. In contrast isolated AuNPs in both functionalized and plasma cleaned states exhibited zero blinking upon excitation at 561 nm and thus were not considered for further studies (Figure S4, Supporting Information). These findings show that aggregation and surface functionalization of AuNPs can ef-

fectively tune their photophysical properties, making them suitable as probes for super-resolution microscopy. In addition these probes can be used in the absence of oxygen scavenging systems, typically required for avoiding photobleaching of organic dyes.<sup>[13]</sup> Among all types of AuNPs studied, the most promising candidates for use as photoswitching emitters in super-resolution imaging were the BPEI-aggregated AuNPs. They exhibited a relatively low duty cycle and high photon numbers per blinking event compared to other functionalized and plasma-cleaned AuNPs. Specifically, BPEI-aggregated AuNPs show an average photon number per blinking event approximately three times higher than Alexa 647, a dye typically used in STORM experiments, while maintaining comparable duty cycles.<sup>[9]</sup> These results demonstrate the versatility of AuNPs compared to small dye molecules; they possess the essential properties for super-resolution imaging, including robust blinking behavior under ambient conditions and low duty cycles, without requiring an oxygen scavenging system.

The analysis of the point spread function (PSF) is a crucial step in determining the resolution of an imaging method. Additionally, the PSF provides a comprehensive three-dimensional view of how light emission is spatially distributed around the AuNPs used in this study. To evaluate the quality of our super-resolution imaging method and the isotropic emission of the AuNPs, we measured the PSF in XYZ directions. First, the diffraction-limited PSF of citrate-functionalized AuNPs was

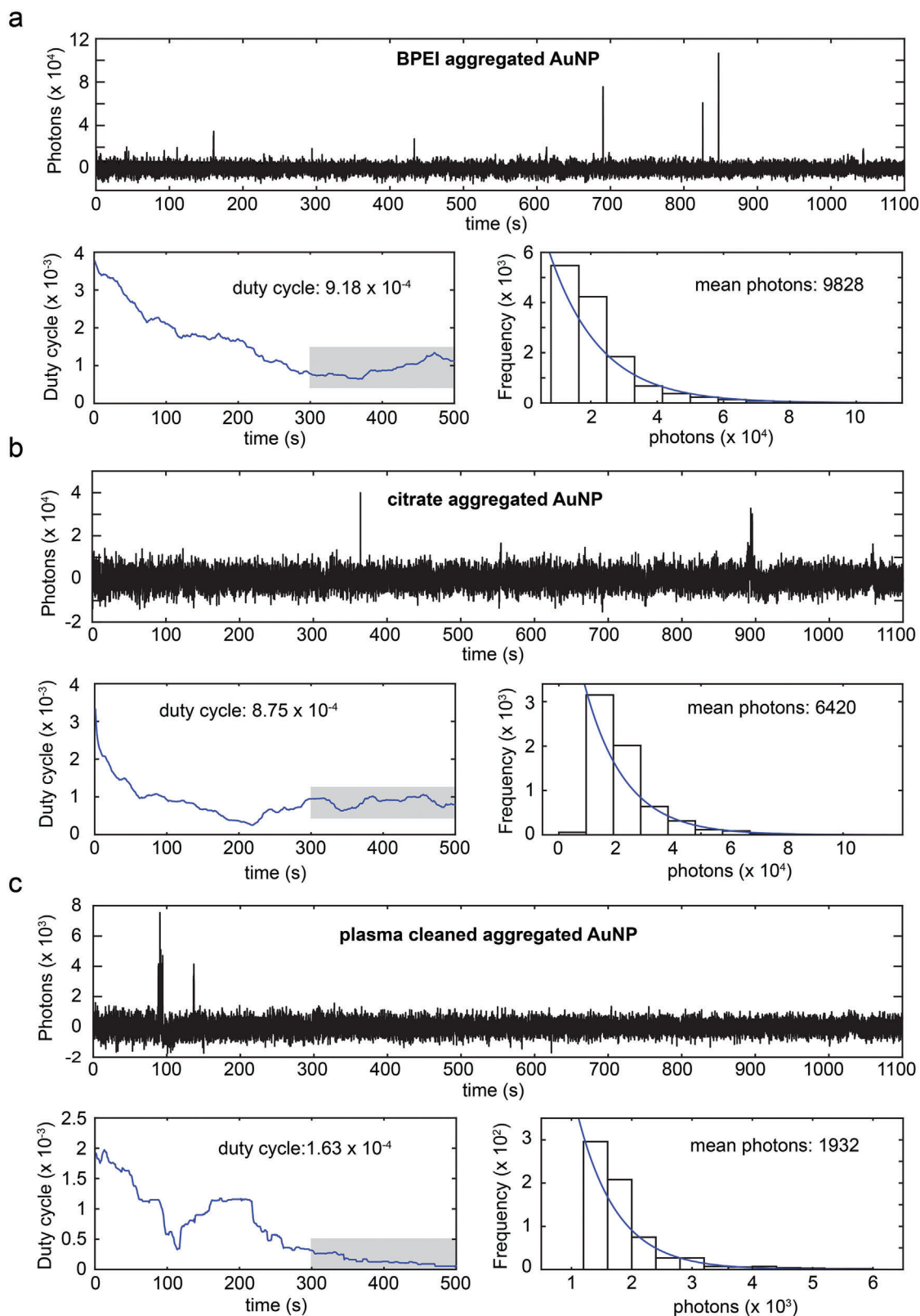


**Figure 3.** Blinking properties of different functionalized AuNPs. Single-NP photoluminescence time traces of a) functionalized-BPEI, b) -citrate, and c) plasma cleaned aggregated AuNPs. In all cases on-off duty cycles (fraction of time a molecule resides in its fluorescent state) were calculated from many single-NPs photoluminescence time traces and plotted over time. The corresponding equilibrium duty cycles were calculated within the time window 300–500 s (gray box). Histogram of the number of photons per blinking event were extracted from single NPs photoluminescence time traces. The mean number of photons was determined from a mono-exponential fit (blue line).

analyzed using TIRF imaging (Figure S5, Supporting Information). The intensity profiles in the X, Y, and Z directions were plotted and found to be well-represented by Gaussian fits. The full width at half maximum (FWHM) values in the X and Y directions were measured to be  $316 \pm 10.8$  and  $320 \pm 17.4$  nm, respectively, while the FWHM in the Z direction was  $562 \pm 24.8$  nm. These measurements confirmed that the X, Y, and Z profiles are diffraction-limited, with the PSF data further demonstrating isotropic intensity profiles in all directions.

To investigate the 3D localization of the blinking AuNPs, we performed 3D STORM reconstruction of the same sample (Figure S6, Supporting Information) using a previously described method.<sup>[51]</sup> Briefly, adaptive optics were introduced into the emission optical path, causing fluorescent particles to appear as elongated spots along either the X or Y direction, depending on their axial (Z) position. The Z coordinate was thus encoded in the ellipticity of each spot and could be computationally retrieved. The reconstructed 3D localization provided FWHM values of  $23.8 \pm 0.55$  nm (X),  $21.4 \pm 0.28$  nm (Y), and  $122.0 \pm 2.39$  nm (Z). Both the diffraction-limited PSF and the 3D localization measurements confirmed that the AuNPs exhibit an isotropic emission profile, consistent with prior findings.<sup>[52]</sup>

## 2.2. Gold Nanoparticles for Super-Resolution Imaging of Nanostructures

As a proof-of-concept of using AuNPs for super-resolution imaging we prepared nanoscale structures on glass and imaged them with a Nikon N-STORM in either TIRF or HILO mode depending on the sample. For samples cast on a glass coverslip or a glass slide, we acquired super-resolution images using either the TIRF or HILO mode, respectively. Nanofabrication procedures to create well-defined nano-structures for the determination of the resolution limit were performed as reported previously.<sup>[53]</sup> Briefly, an elongated silicone rubber sheet was initially plasma etched, which formed a hard nanoscale surface layer. Upon release, relaxation-induced wrinkles with controllable wavelengths emerged, creating parallel lines  $\approx 500$  nm wide.<sup>[54]</sup> It is worth to note that the nanoscale films produce wrinkles that have a periodic wave pattern and thus their reported width was measured from peak to peak (Figure S7, Supporting Information). These nanostructures were then filled with BPEI functionalized aggregated AuNPs. The successful integration of AuNPs into the nanostructures was confirmed using scanning electron microscopy (SEM) and electron-based X-ray emission spectroscopy (EDX) for elemental mapping (Figure 4a,b). Using conventional fluorescence or brightfield imaging these nanostructures could not be resolved as shown in Figure 4c,d. Super-resolution imaging of aggregated nanoparticles confined in these nanostructures was performed using an N-STORM microscope in TIRF mode with a 561 nm laser illumination ( $0.3 \text{ kW cm}^{-2}$  on-sample intensity).

A total of 20 000 frames were acquired for each dataset and subsequently analyzed using super-resolution radial fluctuation (SRRF), an algorithm that processes a sequence of images to generate a super-resolution image directly, bypassing the need for fluorophore localization.<sup>[3]</sup> When fluorophores overlap by a distance smaller than the PSF width, STORM analysis can re-

solve this by ensuring that individual fluorophores appear independently in different frames. However, if fluorophores repeatedly overlap in all frames, this prevents their successful identification as separate entities, potentially leading to their exclusion from the analysis entirely. This issue is analogous to our scenario, where aggregated AuNPs create overlapping conditions. SRRF addresses this challenge by generating probability maps that indicate the likely locations of molecules based on their radial and temporal properties, rather than attempting to localize individual molecules. A plot profile of the reconstructed image (Figure 4e), fitted with a simple Gaussian function, indicated FWHM values of  $105 \pm 10$  nm (Figure 4f). This shows that at the current nanoparticle densities, super-resolution imaging based on AuNP probes can achieve a resolution  $\approx 3\times$  less than the theoretical Abbe's diffraction limit of the emission wavelength ( $\approx 300$  nm for 600 nm emission wavelength). To the best of our knowledge, these data represent the first super-resolution images of lithographically fabricated nanostructures using AuNP aggregates.

An ETH logo ( $3 \times 1.5 \times 0.15 \mu\text{m}^3$ ) with a line width of 150 nm was created by utilizing focused ion beam (FIB) technology (Figure 4g; see Supporting Information and Figure S8, Supporting Information). The reconstructed SRRF image in Figure 4j clearly displays higher resolution than brightfield and HILO fluorescence microscopy images (Figure 4h,i) in agreement with the SEM image (Figure 4g). In addition, the resolution obtained with the SRRF method was substantially improved compared to conventional diffraction-limited confocal imaging (Figure 4j,k) and is comparable to the Airyscan-corrected image (Figure 4j,l). However, due to the high abundance of aggregates, the Airyscan-based super-resolution method is unable to properly resolve the letter H (Figure 4l). These results clearly suggest that aggregated AuNPs can work as probes for super-resolution imaging of nanostructures in air.

## 3. Conclusion

In this study, the emission and blinking properties of AuNPs in two different conditions (isolated and aggregated) and with three different surface functionalizations (BPEI, citrate and no surface functionalization) were investigated. Aggregation of AuNPs, whether functionalized with BPEI or citrate, results in significant changes in their absorbance spectra. Specifically, a redshift and broadening of the plasmon absorption band occur upon aggregation, accompanied by increased absorption in the 600–800 nm range. This spectral evolution indicates strong interparticle interactions due to proximity, enhancing the plasmonic coupling between adjacent nanoparticles. We then demonstrated the role of surface functionalization, with BPEI and citrate, in enhancing the photoluminescence intensity of AuNPs through ligand-metal charge transfer interactions. Citrate-functionalized AuNPs show enhanced PL signals compared to plasma-cleaned and BPEI-functionalized counterparts. This enhancement was attributed to the transfer of charge from electron-rich citrate groups to the metal core via Au-S bonds, facilitating more efficient radiative processes. In addition, time-resolved fluorescence spectroscopy reveals distinct decay components in PL lifetimes of both isolated and aggregated AuNPs. Aggregated AuNPs exhibit longer PL lifetimes compared to their isolated counterparts, suggesting that aggregation alters the local environment around AuNPs,

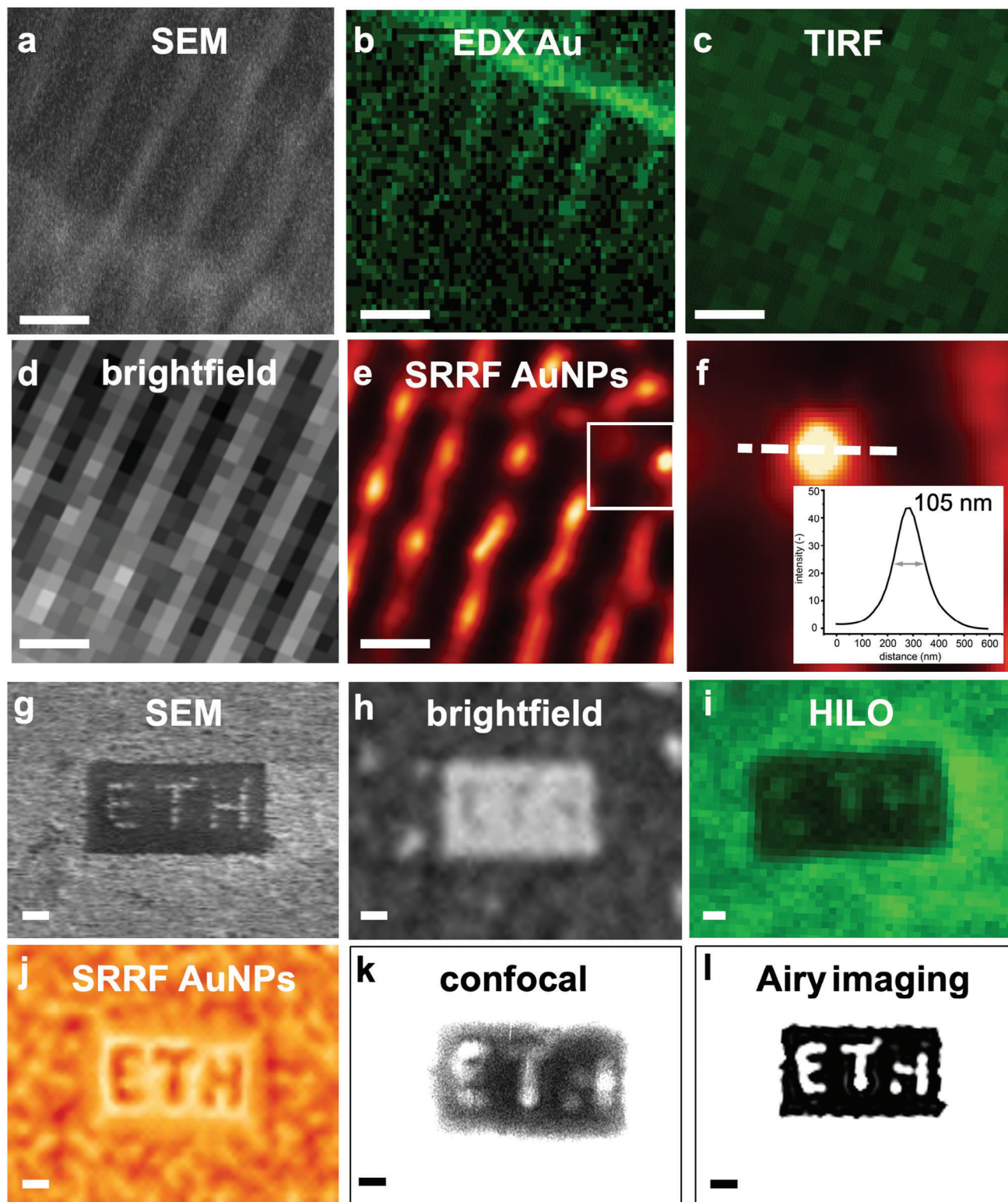


**Figure 4.** Comparison of conventional TIRF and HILO with SRRF imaging of defined nanostructures. a) Imaging nanostructured parallel lines using SEM, b) energy dispersive X-ray spectroscopy (EDX) elemental mapping, c) TIRF imaging, d) brightfield imaging, and e) SR imaging using reconstructions from SRRF. f) Zoomed-in view image as indicated in the white region in (e). The image intensity was fitted with a simple Gaussian function for determining the FWHM of 105 nm, which was used as the resolution for AuNPs-based SRRF imaging. Compared to the images taken by conventional microscopy, where dense parallel lines are not resolvable, the structure and organization of these structures when filled with AuNPs and after SRRF are much clearer and better resolved. Images of ETH logo acquired using g) SEM, h) brightfield imaging, i) HILO imaging, j) SRRF imaging, k) confocal microscopy, and l) Airyscan post processed reconstruction imaging. Images captured with Airyscan achieve resolution values comparable to SRRF but fail to fully resolve the logo due to the high prevalence of aggregates. Scale bar: 500 nm.

significantly affecting their PL decay dynamics. Evaluation of blinking behavior reveals that only aggregated AuNPs, whether functionalized or plasma-cleaned, exhibit robust blinking suitable for super-resolution imaging applications. BPEI-functionalized aggregated AuNPs, in particular, demonstrate high photon intensities per blinking event and low on/off duty cycles, making them promising candidates for photoswitchable emitters in super-resolution microscopy. In contrast, isolated AuNPs in both functionalized and plasma-cleaned states show low photon intensities upon excitation at 561 nm, rendering them unsuitable as super-resolution probes. We successfully leveraged the high photon intensities of aggregated BPEI-coated AuNPs to label nanostructures for super-resolution measurements. Experimental validation using AuNP-coated nanostructures combined with SRRF analysis confirms the feasibility of using BPEI-aggregated AuNPs for achieving super-resolution imaging. The obtained resolution of  $\approx 105$  nm FWHM exceeds diffraction limits, highlighting the potential of AuNPs in surpassing the limitations of organic dyes in resolving nanoscale structures in air.

Although various techniques have been developed to resolve nanostructures, e.g., X-ray microscopy,<sup>[55]</sup> atomic force microscopy (AFM),<sup>[56]</sup> and electron microscopy (EM), these approaches have limitations regarding their applicability. The current results show the potential of gold nano-objects as labels for super-resolution imaging after careful optimization of various parameters such as inter-particle distance, and surface functionalization. The results of the present study show for the first time that the performance of commercially available AuNPs in super-resolution microscopy is superior to that of fluorescent proteins (with respect to bleaching, photon yield, number of switching cycles).<sup>[9]</sup> This paves the way to explore new labeling methods for super-resolution imaging in air and without the need for specialized buffers typically required when organic dyes are used as labels. This study underscores the versatility and efficacy of AuNPs as advanced probes in super-resolution microscopy, leveraging their unique photo-physical properties which can be finely tuned through aggregation and surface functionalization. These unique characteristics could enable the use of AuNPs in analyzing air-exposed structures, such as in label-free investigations of metal electrodes. Further optimization and deeper understanding of the photo-physical mechanisms governing functionalized and aggregated AuNPs could significantly advance super-resolution imaging in nanotechnology.

## 4. Experimental Section

**Sample Preparation and Characterization:** Spherical AuNPs (40 nm diameter,  $7.2 \times 10^{10}$  particles/mL) with citrate surface functionalization were purchased from Sigma (Darmstadt, Germany). Spherical AuNPs (40 nm diameter,  $1.4 \times 10^{12}$  particles/mL) with BPEI surface functionalization were acquired from nanoComposix (San Diego, USA). BPEI functionalized gold nanorods ( $45 \times 15$  nm<sup>2</sup>,  $1.01 \times 10^{13}$  particles/mL) were also acquired from nanoComposix (San Diego, USA). All particles were normalized to a concentration of  $7.2 \times 10^{10}$  particles/mL. The size distribution of gold nanoparticles was characterized by transmission electron microscopy (TEM) (Figure S9, Supporting Information).

Isolated nanoparticles samples were obtained by drop-casting the solution (30  $\mu$ L) onto a clean glass slide (Carl Roth, Karlsruhe, Germany)

and flushing it with a speed of 2–3 mm s<sup>-1</sup> over the glass slide. Significant spacing of the AuNPs was confirmed by scanning electron microscopy (SEM), (Titan Themis, FEI, Hillsboro, USA) (Figure S1a, Supporting Information). For aggregated samples, a drop (30  $\mu$ L) was allowed to dry on clean glass slides, whereby the coffee ring effect<sup>[57]</sup> caused an increased number of particles at the drop borders (Figure S1b, Supporting Information). For more details about the samples' preparation for time resolved photoluminescence and super-resolution measurements, see Text S1 (Supporting Information), Supplementary Materials and Methods and Figures S1 and S8 (Supporting Information). A TEM (Tecnai F20, FEI, Hillsboro, USA) was used to acquire electron micrographs operated at 200 kV. Micrographs from this device were taken using a 2k charge-coupled device camera.

**Photoluminescence Decay Measurements:** Photoluminescence lifetime decays and time integrated photoluminescence measurements were measured with a custom-built confocal time-correlated single photon counting (TCSPC) set-up (Figure S10, Supporting Information). Excitation light of a 405 nm picosecond-pulsed diode laser (QuixX 405-120 PS, Omicron-Laserage Laserprodukte GmbH, Rodgau-Dudenhofen, Germany) was coupled with a fiber delivery system and focused on the sample through a 40 $\times$  magnification microscope objective (40 $\times$  CFI S Plan Fluor ELWD ADM 40XC, 0.60 NA, Nikon, Tokyo, Japan). Photoluminescence from the sample was collected through the same objective and reflected by a dichroic mirror (Laser Beamsplitter HC BS R405, Semrock, Rochester, USA). The residual excitation light was filtered by a long-pass filter (405 LP Edge Basic Longpass Filter, Semrock, Rochester, USA) and reflected by a mirror to the detection path. Photoluminescence was then focused on a 30  $\mu$ m pinhole (P30S Mounted Precision Pinhole, Thorlabs, Dachau, Germany) to reject out-of-focus light. The photoluminescence is then split evenly by a 50:50 beamsplitter (BS031 – 50:50 Non-Polarizing Beamsplitter Cube, Thorlabs). One of the beams was focused on a single photon avalanche photodiode detector (MPD PDM Series 50  $\mu$ m, Micro Photon Devices, Bolzano, Italy) for fluorescence lifetime measurements while the other 50% was used for time-integrated photoluminescence measurements. The avalanche photodiode was connected to a TimeHarp 260 acquisition card (PicoQuant GmbH, Berlin, Germany) with a temporal resolution of 25 ps. The photon pulses of the picosecond laser were repeated at a rate of 20 MHz. Photoluminescence measurements were performed using the same excitation laser source as above but in continuous mode operated at 120 mW. The emission light was focused by a 10 $\times$  magnification objective (RMS10 $\times$  – 10 $\times$  Olympus Plan Achromat Objective, 0.25 NA, 10.6 mm WD, Thorlabs, Dachau, Germany) on a fiber-based spectrometer (QE Pro, Ocean Optics, Largo, USA, or StartLine Avaspec-UJS2048L-EVO, Avantes, Apeldoorn, Netherlands). Measurements were integrated for 10 seconds. A precision motorized stage (Micro-Drive, Mad City Labs, Madison, USA) controlled by Labview software enabled accurate positioning of the laser beam within the AuNPs sample.

**Super-Resolution Measurements and Blinking Time Traces:** A Nikon N-STORM (Nikon, Zurich, Switzerland) was used to record blinking time traces. This device is based on a Nikon Eclipse Ti2 wide field inverted microscope. The laser source wavelength of 561 nm laser was used to excite d-band electrons and the electrons in the plasmon, respectively. The device is equipped with a Nikon Ti-LAPP unit, which allows adjustment of the illumination angle for EPI-fluorescence to total internal reflection fluorescence (TIRF) and highly inclined (HiLO). This device utilized an Apochromat TIRF 100 $\times$  NA = 1.49 oil immersion objective (Nikon, Zurich, Switzerland). The utilized camera was an EM-CCD camera (ANDOR iXon DU897, Oxford Instruments, Abingdon, UK). Depending on the sample support being a glass slide or coverslip, different holders and therefore different observation modes (TIRF and HILO respectively) were used. All measurements were performed at an intensity of 100% excitation power which for 561 nm laser excitation was  $1.5 \times 10^6$  W/m<sup>2</sup>. All images were acquired at a field of view of 128 $\times$ 128 pixels at 20 fps. In the case of 3D super-resolution PSF measurements, the images were reconstructed using STORM. All other super-resolution images were reconstructed using the SRRF algorithm.<sup>[3]</sup> The SRRF algorithm, is a freely available ImageJ plugin named NanoJ-SRRF. More specifically from the SRRF analysis dialog box, the Temporal Radiality Pairwise Product Mean (TRPPM) method

was used for the temporal analysis side of the algorithm, the calculation of the radially transform and the weighting.

**Blinking Properties Characterization:** For each sample, 20 000 consecutive frames were recorded under continuous excitation by a laser at 561 nm at 10 ms exposure time. To generate single-nanoparticle blinking traces, the nanoparticles were localized and then single nanoparticle blinking traces were generated from background corrected intensities for each localization, using a custom MATLAB script. The number of photons emitted for each blinking event was determined and used to generate the histograms of photons per blinking events. The reported mean values were extracted from a single-exponential fit. The on-off duty cycle corresponds to the fraction of time that the nano-object resides in its on (emitting) state and was calculated over a sliding window of 200 s, according the method of Dempsey et al.<sup>[9]</sup>

**Airyscan and Confocal Measurements:** For comparison with STORM and SRRF, Airyscan and confocal microscopy was performed using a Zeiss LSM 880 Airyscan microscope (Carl Zeiss Microscopy, Oberkochen, Germany) equipped with a 63× 1.4NA Oil DIC Plan- Aplanochromat objective and the sample was excited at 561 nm.

## Supporting Information

Supporting Information is available from the Wiley Online Library or from the author.

## Acknowledgements

The authors gratefully acknowledge the support from the National Natural Science Foundation of China (Grant No.: 22172043) provided to J.F., and from ETH Zürich. J.F. also thanks HIT for facilitating his academic visit to ETH. Additionally, S.S. expresses his gratitude to Andrew deMello for generously providing essential resources for this project. The authors would like to thank Dr. Dorothea Pinotsi from the Scientific Center for Optical and Electron Microscopy (ScopeM) at ETH Zurich for her help in super-resolution imaging.

## Conflict of Interest

The authors declare no conflict of interest.

## Author Contributions

J.P. and P.M. contributed equally to this work. J.P. performed all photoluminescence and time resolved measurements. P.M. performed the analysis of lifetime and photoblinking measurements and conducted super-resolution measurements. M.G. conducted preliminary measurements. T.S. and Q.H. contributed to the implementation of the research. G.C. provided experimental support. H.G. performed SEM measurements and carbon sputtering of the samples. A.V.S. contributed to the design of the research. M.K. manufactured the nanostructured samples. G.Q. performed preliminary experiments. J.W. contributed to the implementation of the research. J.F. conceived the original idea and performed super-resolution measurements. S.S. supervised the project, interpreted the results, and wrote the manuscript.

## Data Availability Statement

The data that support the findings of this study are available from the corresponding author upon reasonable request.

## Keywords

blinking fluorophores, fluorescence imaging, fluorescence lifetime imaging, gold nanoparticles, super resolution imaging

Received: August 31, 2024

Revised: December 17, 2024

Published online:

- [1] E. Abbe, *J. R. Soc. Interface* **1881**, 1, 388.
- [2] E. Betzig, G. H. Patterson, R. Sougrat, O. W. Lindwasser, S. Olenych, J. S. Bonifacio, M. W. Davidson, J. Lippincott-Schwartz, H. F. Hess, *Science* **2006**, 313, 1642.
- [3] N. Gustafsson, S. Culley, G. Ashdown, D. M. Owen, P. M. Pereira, R. Henriques, *Nat. Commun.* **2016**, 7, 12471.
- [4] D. T. Burnette, P. Sengupta, Y. Dai, J. Lippincott-Schwartz, B. Kachar, *Proc. Natl. Acad. Sci. USA* **2011**, 108, 21081.
- [5] M. J. Rust, M. Bates, X. W. Zhuang, *Nat. Methods* **2006**, 3, 793.
- [6] T. Dertinger, M. Heilemann, R. Vogel, M. Sauer, S. Weiss, *Angew. Chem., Int. Ed* **2010**, 49, 9441.
- [7] S. T. Hess, T. P. K. Girirajan, M. D. Mason, *Biophys. J* **2006**, 91, 4258.
- [8] M. Ovesný, P. Křížek, J. Borkovec, Z. Svindrych, G. M. Hagen, *Bioinformatics* **2014**, 30, 2389.
- [9] G. T. Dempsey, J. C. Vaughan, K. H. Chen, M. Bates, X. Zhuang, *Nat. Methods* **2011**, 8, 1027.
- [10] P. Bharadwaj, L. Novotny, *Nano Lett* **2011**, 11, 2137.
- [11] C. E. Aitken, R. A. Marshall, J. D. Puglisi, *Biophys. J.* **2008**, 94, 1826.
- [12] L. Nahidiazar, A. V. Agronskaia, J. Broertjes, B. Den Van Broek, K. Jalink, *PLoS ONE* **2016**, 11, 0158884.
- [13] M. Swoboda, J. Henig, H. M. Cheng, D. Brugger, D. Haltrich, N. Plumeré, M. Schlierf, *ACS Nano* **2012**, 6, 6364.
- [14] Y. Wang, G. Fruhwirth, E. Cai, T. Ng, P. R. Selvin, *Nano Lett.* **2013**, 13, 5233.
- [15] X. Yang, K. Zhanghao, H. Wang, Y. Liu, F. Wang, X. Zhang, K. Shi, J. Gao, D. Jin, P. Xi, *ACS Photonics* **2016**, 3, 1611.
- [16] O. Mandula, I. Š. Šestak, R. Heintzmann, C. K. I. Williams, *Opt. Express* **2014**, 22, 24594.
- [17] M. Heilemann, S. Van De Linde, M. Schüttel, R. Kasper, B. Seefeldt, A. Mukherjee, P. Tinnefeld, M. Sauer, *Angew. Chem., Int. Ed.* **2008**, 47, 6172.
- [18] G. H. Patterson, J. Lippincott-Schwartz, *Science* **2002**, 297, 1873.
- [19] M. Schwing, A. Kiel, A. Kurz, K. Lympopoulos, A. Sprödfeld, R. Krämer, D.-P. Herten, *Angew. Chem., Int. Ed.* **2011**, 50, 2940.
- [20] A. Sharonov, R. M. Hochstrasser, *Proc. Natl. Acad. Sci. USA* **2006**, 103, 18911.
- [21] D. Wöll, C. Flors, *Small Methods* **2017**, 1, 1700191.
- [22] X. Liu, S.-Y. Chen, Q. Chen, X. Yao, M. Gelléri, S. Ritz, S. Kumar, C. Cremer, K. Landfester, K. Müllen, S. H. Parekh, A. Narita, M. Bonn, *Angew. Chem., Int. Ed.* **2020**, 59, 496.
- [23] O. Nevskiy, D. Sysoiev, J. Dreier, S. C. Stein, A. Oppermann, F. Lemken, T. Janke, J. Enderlein, I. Testa, T. Huhn, D. Wöll, *Small* **2018**, 14, 1703333.
- [24] A. Mooradian, *Phys. Rev. Lett.* **1969**, 22, 185.
- [25] C. D. Geddes, A. Parfenov, I. Gryczynski, J. R. Lakowicz, *Chem. Phys. Lett.* **2003**, 380, 269.
- [26] M. Eghtedari, A. V. Liopo, J. A. Copland, A. A. Oraevsky, M. Motamedi, *Nano Lett* **2009**, 9, 287.
- [27] N. L. Rosi, C. A. Mirkin, *Chem. Rev.* **2005**, 105, 1547.
- [28] C. Yang, Y. Wang, J.-L. Marty, X. Yang, *Biosens. Bioelectron.* **2011**, 26, 2724.
- [29] H. He, C. Xie, J. Ren, *Anal. Chem.* **2008**, 80, 5951.
- [30] M. Bates, B. Huang, X. Zhuang, *Curr. Chem. Biol.* **2008**, 12, 505.
- [31] W. Haiss, N. T. K. Thanh, J. Aveyard, D. G. Fernig, *Anal. Chem.* **2007**, 79, 4215.
- [32] P. Apell, R. Monreal, S. Lundqvist, *Phys. Scr.* **1988**, 38, 174.
- [33] E. Minutella, F. Schulz, H. Lange, *J. Phys. Chem. Lett.* **2017**, 8, 4925.

- [34] M. Yorulmaz, S. Nizzero, A. Hoggard, L.-Y. Wang, Y.-Y. Cai, M.-N. Su, W.-S. Chang, S. Link, *Nano Lett.* **2015**, *15*, 3041.
- [35] S. Peng, J. M. McMahon, G. C. Schatz, S. K. Gray, Y. Sun, *Proc. Natl. Acad. Sci. USA* **2010**, *107*, 14530.
- [36] W. He, J. Frueh, Z. Wu, Q. He, *Langmuir* **2016**, *32*, 3637.
- [37] Z. Ebrahimpour, N. Mansour, *Plasmonics* **2018**, *13*, 1335.
- [38] A. K. Tiwari, M. K. Gupta, R. Meena, P. C. Pandey, R. J. Narayan, *Sensors* **2024**, *24*, 2169.
- [39] Z. Wu, R. Jin, *Nano Letters* **2010**, *10*, 2568.
- [40] S. K. Ghosh, T. Pal, *Chem. Rev.* **2007**, *107*, 4797.
- [41] P. K. Jain, W. Huang, M. A. El-sayed, *Nano Lett.* **2007**, *7*, 2080.
- [42] G. V. Hartland, *Chem. Rev.* **2011**, *111*, 3858.
- [43] H. Liao, J. H. Hafner, *Chem. Mater.* **2005**, *17*, 4636.
- [44] Y. Zhang, J. Yu, D. J. S. Birch, Y. Chen, *J. Biomed. Opt.* **2010**, *15*, 020504.
- [45] S. Suarasan, E. Licarete, S. Astilean, A.-M. Craciun, *Colloids Surf. B: Biointerfaces* **2018**, *166*, 135.
- [46] K. Imura, T. Nagahara, H. Okamoto, *J. Phys. Chem. B* **2005**, *109*, 13214.
- [47] D. Huang, C. P. Byers, L.-Y. Wang, A. Hoggard, B. Hoener, S. Dominguez-Medina, S. Chen, W.-S. Chang, C. F. Landes, S. Link, *ACS Nano* **2015**, *9*, 7072.
- [48] M. B. Mohamed, V. Volkov, S. Link, M. A. El-Sayed, *Chem. Phys. Lett.* **2000**, *317*, 517.
- [49] Z. Luo, X. Yuan, Y. Yu, Q. Zhang, D. T. Leong, J. Y. Lee, J. Xie, *J. Am. Chem. Soc.* **2012**, *134*, 16662.
- [50] A. Beveratos, R. Brouri, T. Gacoin, J.-P. Poizat, P. Grangier, *Phys. Rev. A* **2001**, *64*, 061802.
- [51] B. Huang, W. Wang, M. Bates, X. Zhuang, *Science* **2008**, *319*, 810.
- [52] J. Pettine, S. M. Meyer, F. Medeghini, C. J. Murphy, D. J. Nesbitt, *ACS Nano* **2021**, *15*, 1566.
- [53] A. M. Steiner, M. Mayer, M. Seuss, S. Nikolov, K. D. Harris, A. Alexeev, C. Kuttner, T. A. F. König, A. Fery, *ACS Nano* **2017**, *11*, 8871.
- [54] A. Schweikart, A. Fery, *Microchim. Acta* **2009**, *165*, 249.
- [55] A. Sakdinawat, D. Attwood, *Nat. Photonics* **2010**, *4*, 840.
- [56] F. J. Giessibl, *Rev. Mod. Phys.* **2003**, *75*, 949.
- [57] R. D. Deegan, O. Bakajin, T. F. Dupont, G. Huber, S. R. Nagel, T. A. Witten, *Nature* **1997**, *389*, 827.